Optimization of growth and ordering of Ag nanoparticle arrays on ripple patterned alumina surfaces for strong plasmonic coupling

Sophie Camelio, Elliot Vandenhecke, Sophie Rousselet, David Babonneau

Optimization of growth and ordering of Ag nanoparticle arrays on ripple patterned alumina surfaces for strong plasmonic coupling

S Camelio*, E Vandenhecke, S Rousselet and D Babonneau

Institut Pprime, Département Physique et Mécanique des Matériaux, UPR 3346 CNRS, Université de Poitiers, SP2MI, Téléport 2 – 11 Bvd. M. et P. Curie, BP 30179, 86962 Futuroscope Chasseneuil Cedex, France

sophie.camelio@univ-poitiers.fr

Abstract. Low-energy ion beam sputtering of alumina thin films followed by growth of metallic nanoparticles by glancing angle deposition is optimized in order to produce arrays of silver nanoparticle chains with a strong plasmonic dichroism. A systematic study is undertaken in order to establish the influence of the angle of silver deposition and the ordering of the pre-patterned rippled surface on the morphology and organization of the nanoparticles, and on their associated optical properties. High ion fluence for ripple formation and low glancing angle for metal deposition favor the formation of aligned and elongated particles with sub-nanometer gaps. Numerical simulations show that these nanoparticle arrays generate high electric field enhancements for an excitation parallel to the particle chains, and therefore can be used for surface enhanced spectroscopies.

PACS: 81.16.Rf, 81.16.-c, 78.67.Bf

1. Introduction

In recent years, many groups have been working on the preparation of arrays of metallic nanoparticles that have the peculiarity to present localized surface plasmon resonances (LSPR), i.e. collective oscillations of the conduction electrons, associated with electric field amplification in the immediate vicinity of the nanoparticles [1-3]. The spectral position and magnitude of the LSPR not only depend on the intrinsic properties of the metal and dielectric environment of the particles, but also on their

morphology (shape and size) and their spatial organization [1-4]. These arrays can find applications as light absorbers, sensors, and more especially as active surfaces for surface enhanced Raman scattering (SERS) or metal enhanced fluorescence experiments [5-7]. Indeed, the extraordinary intense local field enhancement present in the gaps between closely spaced nanoparticles, known as hot-spots, induces an intense amplification of the Raman signal so as to reach the detection of very low concentrations of analytes. Nevertheless, improving ease fabrication of active surfaces with high density of narrow gaps (with dimensions less than 5 nm) remains a challenge for industrial applications, i.e. for producing large areas at low cost and at wafer scale. Among the most widely used SERS active substrates are metal colloids generated by chemical methods, which have the advantage of producing nanoparticles with narrow dispersion sizes. However, particle aggregation and hence an imprecise control of nanoparticle distances turn the reproducibility more challenging. A way to overcome this problem is to immobilize the particles on the surface, but adhesion to the surface is usually poor. A physical solution is to use top-down approaches such as traditional nanolithography techniques (electron beam lithography, focused ion beam lithography) that enable to create reproducible arrays of particles with fine control of their size, shape and interparticle gap. The best resolution obtained so far with these techniques is about 20 nm, while sub-10 nm resolution is expected with nanoimprit lithography [6, 8]. Nevertheless, their low throughput and high production cost make them prohibited for large scale production. Previous papers [9-12] have shown how to engineer the surface of a solid by ion-beam sputtering (IBS) at low energy in order to produce, in a one-step process, regular nanoscale patterns such as self-organized unidirectional nanoripples, with period varying from a few nm to several μm and with nanopatterned surface areas up to several cm^2. Subsequent physical vapor deposition of metal at glancing angles onto such nanoripple patterns [13-18] can lead to the formation of elongated nanoparticles with dimensions and gaps below the resolution of lithographic techniques, and therefore high density of hot spots responsible for a stronger SERS signal compared to non-ordered nanoparticles on a flat substrate [19]. Also, the SERS intensity for light polarized along the nanoparticle chains is much higher than the intensity for light polarized in the transverse direction. However, since the interparticle gap is a key factor to favor a strong electric field enhancement, the spatial organization of the particles just as their shape and size have to be optimized. In this paper, a systematic study is undertaken to establish the influence of the angle of silver deposition and ripple ordering on the growth of silver nanoparticles on rippled alumina surfaces. Moreover, numerical simulations evidence the strong influence of gap value and number of nanoparticles within a chain on the electric field enhancement. Hence, the structural parameters of the particles, correlated to their optical properties (position and width of their LSPR) enable us to optimize the elaboration conditions in order to obtain high density ($> 10^{11}$ cm^{-2}) of sub-nanometer gaps for strong plasmonic coupling.

2. Experimental

Our samples consist of Ag nanoparticles sandwiched between two amorphous Al_2O_3 films. Their preparation was carried out by alternate ion beam sputtering in a Nordiko™ 3000 vacuum chamber and has been depicted in detail elsewhere [16]. Rippled surfaces were produced on amorphous Al_2O_3 films by IBS with Xe^+ ions at a sputtering angle of 55° with respect to the surface normal, at room temperature (RT), and at a constant ion flux in the range of 10^{15} ions cm^{-2} s^{-1}. It is well known that the generation of ripple patterns by IBS, and more especially the ripple period as well as the pattern quality, strongly depend on the sputtering conditions (ion energy and mass, total fluence, angle of incidence, temperature, etc.) [9-12]. In this paper, the period and ordering of the ripples were adjusted by varying the sputtering time (i.e. ion fluence) and the ion energy (table 1) as presented in section 3.1.

The pre-patterned Al_2O_3 surfaces were used as templates for the subsequent growth of Ag nanoparticles by glancing angle deposition at RT. The effects of deposition angle (section 3.2) were studied from samples with Ag being deposited at different glancing angles (90°, 20°, 8° and 2° with respect to the mean surface) in the direction perpendicular to ripples formed by 1 keV-Xe^+ IBS of Al_2O_3 surfaces during 300 s. The Ag deposition time (τ_{Ag}) was calibrated to ensure an almost constant Ag equivalent thickness (t_{Ag}) whatever the deposition angle; whereas Rutherford Backscattering Spectrometry (RBS) measurements were performed to estimate the corresponding t_{Ag} variations (table 2). To study the influence of the ripple ordering (section 3.3), Ag depositions at a glancing angle of 2° were performed (t_{Ag} = 1.4 nm) on pre-patterned Al_2O_3 surfaces prepared by 1 keV-Xe^+ IBS during 100 s and 600 eV-Xe^+ IBS with different sputtering times (100 s, 200 s, 500 s and 1000 s). In all cases, a thin Al_2O_3 capping-layer was finally deposited at RT on the Ag nanoparticles to prevent ageing effects and/or contamination.

All the samples were made onto silicon substrates for Atomic Force Microscopy (AFM) and grazing incidence small-angle x-ray scattering (GISAXS) characterizations, fused silica substrates for optical measurements, and NaCl single crystals for high-angle annular dark-field scanning transmission electron microscopy (HAADF-STEM) observations. The samples prepared onto NaCl single crystals were floated in purified water and the resulting freestanding thin films were collected on microscope copper grids. The morphology and ordering of the pre-patterned surfaces was characterized by AFM using a Nanoscope Digital instrument in the tapping mode. The morphology and spatial organization of the nanoparticles were analyzed from in-plane views by HAADF-STEM with a JEOL 2200FS microscope using an acceleration voltage of 200 kV, a probe size of 0.7 nm, and an inner collection angle of 50 mrad. Selected samples were also studied in the reciprocal space by GISAXS. This "nonlocal" technique is an ideal complementary tool to observe surface modifications induced by IBS and growth of particles on such surfaces since it probes large areas, up to several mm^2, and therefore

gives statistical information [20]. The GISAXS data were collected at the European Synchrotron Radiation Facility (Grenoble, France) with the small-angle scattering setup of the D2AM beamline. The incident X-ray beam (photon energy of 9.8 keV) was parallel to the ripple direction, the incidence angle was close to the critical angle for total external reflection of Al_2O_3 (α_c = 0.214°), and the sample-to-detector distance was 1975 mm. The optical properties were investigated (section 3.4) by means of spectroscopic transmission of polarized light at normal incidence in the spectral range (250 nm - 1200 nm) by using a Cary5000 spectrophotometer from Agilent Technologies equipped with a rotating polarizer. All optical spectra are macroscopic measurements (beam diameter ~ 3 mm).

3. Results

3.1. *Morphology of the pre-patterned surfaces*

Typical surface morphologies of pre-patterned Al_2O_3 thin films with sputtering parameters "ion energy-sputtering time" (600 eV-1000 s), (600 eV-100 s), and (1 keV-100 s), respectively, are shown in figures 1(a)-1(c). As reported in previous papers [16, 17, 18, 20], periodic ripples oriented in the direction perpendicular to the projection of the Xe^+ beam are formed onto the Al_2O_3 surface. At first glance, both the ripple period and the pattern quality are influenced by the sputtering time and ion energy. This is quantitatively confirmed with the 1D Power Spectral Density (PSD) functions of the images presented in figures 1(d)-1(f). From the position and width of the first-order PSD peak, the ripple period Λ and the pattern correlation length ξ can be retrieved [21]. ξ corresponds to the inverse of the full width at half maximum of the first-order PSD peak and gives the length scale up to which positional correlation is present on the surface, i.e. ξ is a measure for the lateral ordering of the ripples The thinner is the peak, the more ordered are the ripples. In table 1, we can notice that the period is increased and the pattern quality is improved with long sputtering times. Furthermore, higher ion energy leads to an increase of the ripple period, while it seems to have little influence on the ripple ordering. These observations are comparable to previous results reported in the literature for insulating surfaces subjected to IBS at RT [22-24]. 2D GISAXS maps obtained for Al_2O_3 thin films sputtered at (600 eV-1000 s) and at (1 keV-100 s) are displayed in figure 2 for comparison. It is worth noting that 1D PSD functions and 2D GISAXS maps exhibit similar features, thus indicating that the 'local' information obtained by AFM on small areas of the order of 1 μm^2 is relevant to the mean surface morphology. Indeed, first and second-order satellite streaks are readily observed by GISAXS, which demonstrates that the formation of unidirectional periodic ripples takes place on the whole surface. Moreover, as a consequence of the loss of ordering as the sputtering time is decreased from 1000 s (figure 2(a)) to 100 s (figure 2(b)), one can notice that the first-order streaks broaden whereas the second-order streaks are strongly attenuated, which qualitatively endorses the conclusions drawn from

the AFM images and corresponding PSD functions. Finally, a ripple height of about 5 nm was estimated from the vertical extension of the scattering streaks [20], thus yielding a mean ripple slope in the range from 20° to 25°.

Table 1: Morphological parameters obtained from AFM measurements on pre-patterned Al_2O_3 thin films with different sputtering parameters (energy of Xe ions and sputtering time): ripple period Λ and normalized correlation length ξ/Λ.

Sputtering energy (eV)	Sputtering time (s)	Λ (nm)	ξ/Λ
600	100	18.7	2.7
	200	20.1	3.6
	500	21.6	5.7
	1000	23.5	6.2
1000	100	23.3	2.3
	300	25.0	4.8

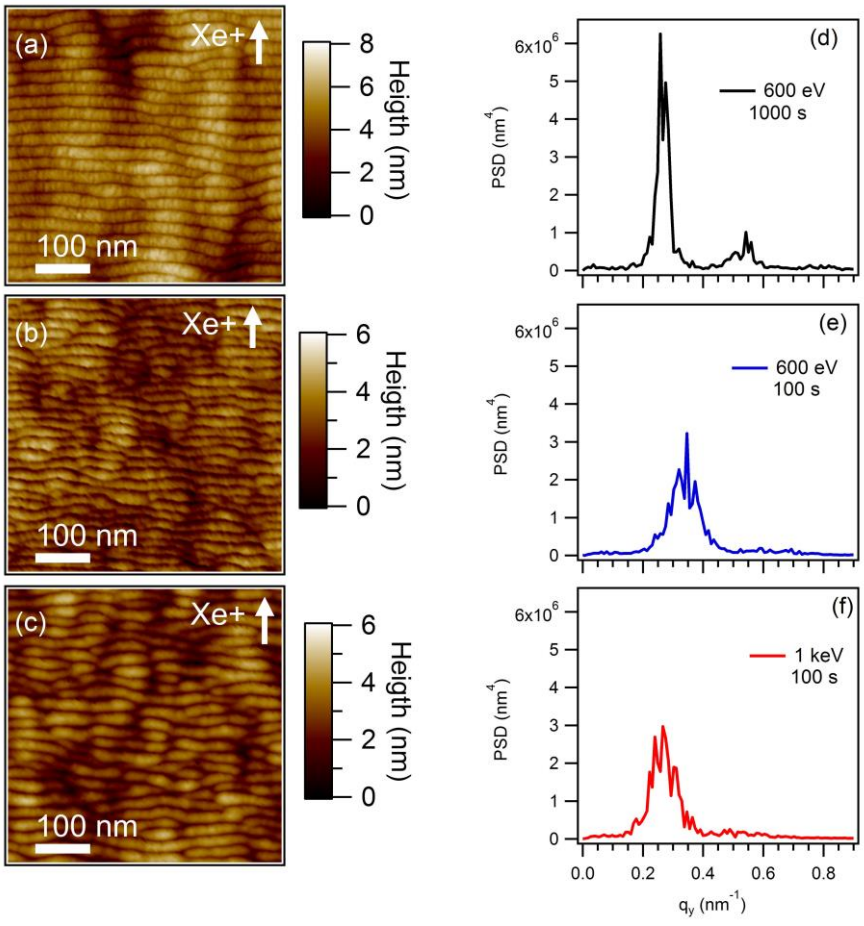

Figure 1: AFM images of the surface morphology obtained for pre-patterned Al_2O_3 thin films with sputtering parameters (a) 600 eV-1000 s, (b) 600 eV-100 s, and (c) 1 keV-100 s. The direction of the Xe^+ beam projection is shown by the arrow. Corresponding 1D PSD functions obtained by Fourier transformation of the AFM images with sputtering parameters (d) 600 eV-1000 s, (e) 600 eV-100 s, and (f) 1 keV-100 s.

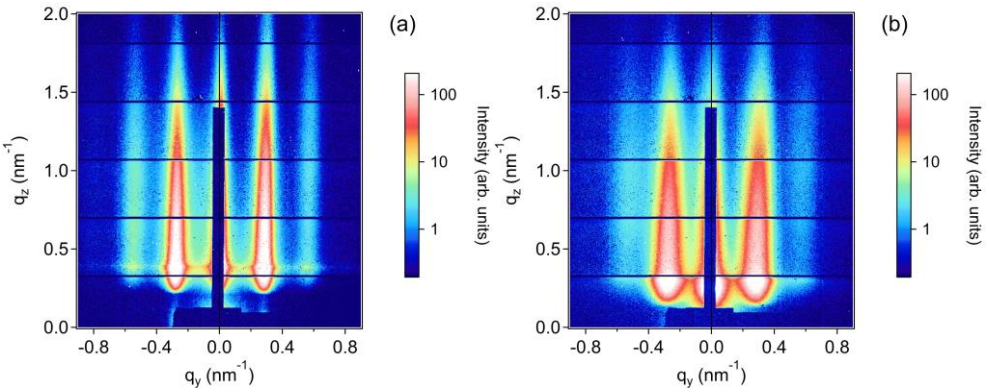

Figure 2: Experimental 2D GISAXS maps obtained for pre-patterned Al_2O_3 thin films with sputtering parameters (a) 600 eV-1000 s and (b) 1 keV-100 s.

3.2. Influence of the Ag deposition angle on the particle morphology and in-plane organization

Figures 3(a)-3(d) show the in-plane organization and the morphology of Ag nanoparticles characterized by HAADF-STEM for samples prepared using different glancing angles of Ag deposition (90°, 20°, 8°, and 2°, respectively) on surfaces patterned with 1 keV ions during 300 s. The particles appear in bright contrast over a dark background corresponding to the signal of the Al_2O_3 matrix. It should be noted that the nucleation of metal nanoparticles obtained by normal incidence deposition onto flat amorphous dielectric surfaces is mainly affected by the density of point defects on the surface whereas their growth is isotropic in average [25, 26]. As a matter of fact, such nanoparticles can be considered as ellipsoids randomly oriented and distributed on the surface. Similarly, despite local variations of the incident metal flux, the seed formation of nanoparticles obtained by glancing angle deposition onto nanorippled amorphous Al_2O_3 takes place on the whole surface because the diffusion length of metal atoms is much larger than the ripple period [17]. Nevertheless, figures 3(a)-3(d) clearly show that the particle growth is more or less anisotropic and is strongly influenced by the angle of deposition.

The HAADF-STEM images presented in figures 3(a)-3(d) were analyzed by digital image processing assuming ellipsoidal nanoparticles (with in-plane long axis a and short axis b) oriented with an angle θ compared to the ripple direction, as shown in figure 4. The resulting in-plane size D (defined as $D = \sqrt{ab}$) distributions are given in figure 5 whereas the in-plane aspect ratios a/b as a function of D and θ are plotted in figure 6. It should be noted that only the particles with $D \geq 1.5$ nm (i.e. larger than twice the probe size) were taken into account. To obtain quantitative information, the size histograms were fitted using a bimodal lognormal distribution defined by two peak positions and full widths at half maximum (fwhm). The derived positions (D_1 and D_2) and fwhm (σ_1 and σ_2) are given in table 2 together with the mean center-to-center distances between the particles in the directions parallel ($L_{//}$) and perpendicular ($L_{\perp}$) to the ripples and the normalized correlation length $\xi_{\perp}/L_{\perp}$ and $\xi_{//}/L_{//}$, which were obtained from the analysis of the autocorrelation functions displayed in figures 3(e)-3(h) and from the PSD functions (not shown), respectively.

As shown in figure 5(a), normal incidence deposition of Ag on the nanorippled surface results in a monomodal D distribution centered at $D_2 = 5.3$ nm. Most of the particles have an ellipsoidal shape with an in-plane size D smaller than 12 nm and an in-plane aspect ratio a/b in the range from 1 to 4 (figure 6(a)). However, a random orientation of the particles with respect to the ripples is observed (figure 6(b)). In this case, the autocorrelation function of the HAADF-STEM image (figure 3(e)) exhibits both an almost circular ring with a radius ~10 nm (typical of an almost isotropic in-plane organization) and weak horizontal fringes with a period ~23.3 nm similar to the ripple period of the pre-patterned Al_2O_3 surface. These results show that, even at normal incidence, local Ag flux variations on the surface (due to the presence of ripples) have an influence on the particle growth, which induces a slight anisotropy in the spatial organization of the particles [18, 27] with $\xi_{\perp}/L_{\perp}$ being a little higher than $\xi_{//}/L_{//}$. Nevertheless, it is clear that the periodic ripple pattern is not fully replicated by the Ag nanoparticles, which grow on the whole surface. Moreover, it is worth noting that the mean gap between adjacent particles in the direction parallel to the ripples can be estimated as $(L_{//} - D_2) = 4.7$ nm, i.e. $(L_{//} - D_2)/D_2 \approx 0.9$. When the glancing angle of Ag deposition is reduced to 20° (i.e. close to the mean ripple slope), the local variations of Ag flux on the rippled surface are amplified, which results in a broadening of both the D (figure 5(b)) and a/b (figure 6(c)) distributions. Furthermore, a broad peak centered at $\theta = 0°$ appears in the a/b vs θ plot (figure 6(d)), whereas the horizontal fringes in the autocorrelation function displayed in figure 3(f) get more pronounced than those observed for normal incidence deposition. The ordering is improved in the perpendicular direction as shown by the increase of $\xi_{\perp}/L_{\perp}$. Thus, deposition at a glancing angle of 20° tends to promote the particle growth in the direction parallel to the ripples, which causes a decrease of the mean gap between adjacent particles with $(L_{//} - D_2) \approx 0.8\, D_2$. At smaller glancing angles of Ag deposition (8° and 2°), the size distribution gradually splits into a bimodal distribution (figures 5(c) and 5(d)), with a narrow

distribution of small nanoparticles centered at $D_1 = 2.5$ nm and a broader distribution of larger particles whose mean size D_2 increases as the deposition angle decreases (table 2). Overall, the nanoparticles smaller than 12 nm present an in-plane aspect ratio $a/b < 3$, with no obvious correlation between a/b and D (figures 6(e) and 6(g)). Furthermore, they are randomly oriented and distributed on the surface (figures 6(f) and 6(h)), as obtained with normal incidence deposition. In contrast, for sizes larger than 12 nm, we observe that a/b increases linearly with D and that such elongated nanoparticles are preferentially aligned along the nanoripples ($\theta = 0°$). Moreover, as shown in figures 3(g) and 3(h), the periodic fringes observed in the corresponding autocorrelation functions get sharper as the deposition angle decreases (with $\xi_\perp / L_\perp$ approaching the value obtained on the pre-patterned surface), suggesting that a replication of the lateral order between ripples is achieved. In these grazing-incidence deposition conditions, the mean distance $L_\perp$ is thus imposed by the ripple period, while the transverse extension of the elongated particles is relatively constant, between 7 and 9 nm. Hence, the particle growth in the transverse direction is limited by the dimension of the ripple sides exposed to the Ag flux whereas the growth of the particles nucleated on the opposite sides is wiped out by shadowing effects. Accordingly, as the glancing angle of deposition is decreased, the particles are more and more elongated in the longitudinal direction due to particle coalescence, which produces an increase of the mean center-to-center distance $L_{//}$ (table 2) together with a decrease of the $(L_{//} - D_2)/D_2$ ratio from 0.59 for Ag deposition at 8° to 0.49 at 2°. Moreover, the particle ordering (i.e. $\xi_{//} / L_{//}$) is still low in this direction. Actually, as a result of the broad size and distance distributions in the longitudinal direction, there exists a broad distribution of gaps between adjacent particles within a chain, with a high density of narrow gaps smaller than 5 nm, as shown in the inset of figure 3(d). Therefore, at very low glancing angles of deposition, shadowing effects associated with low Ag deposition rates cause a preferential growth on the ripple sides exposed to the Ag flux and along the longitudinal direction, which results in the production of nanoparticle arrays consisting of aligned chains of closely spaced elongated nanoparticles, oriented in the ripple direction, with a chain periodicity imposed by the underlying patterned Al_2O_3 surface.

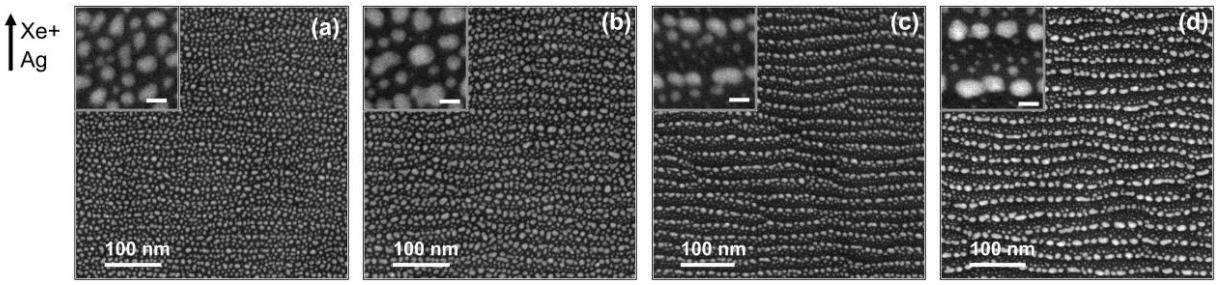

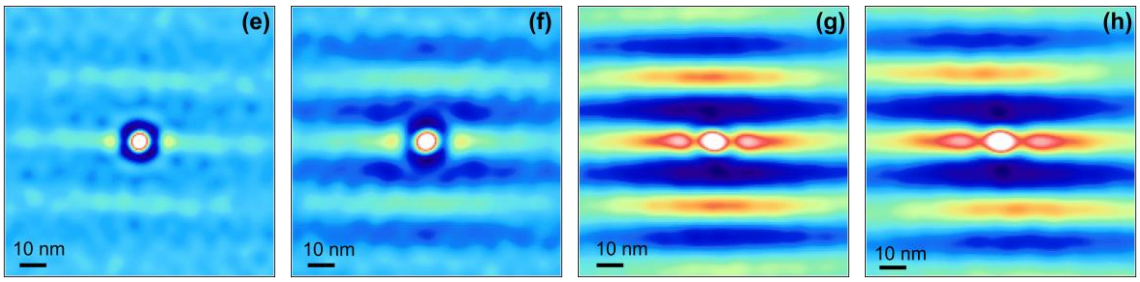

Figure 3: HAADF-STEM plan view images of Al_2O_3-capped Ag nanoparticles grown on rippled Al_2O_3 thin films with different glancing angles for Ag deposition: (a) 90°, (b) 20°, (c) 8° and (d) 2°. Scale bars in the zoomed portions shown in the insets correspond to 10 nm. (e,f,g,h) Corresponding autocorrelation functions of images (a,b,c,d). The direction of the Xe^+ and Ag beam projections are shown by the arrow.

Table 2: Ag deposition time τ_{Ag}, Ag equivalent thickness t_{Ag} obtained from RBS measurements, and structural parameters retrieved from the quantitative analysis of HAADF-STEM images and corresponding autocorrelation functions of Al_2O_3-capped Ag nanoparticles grown on rippled Al_2O_3 thin films with different glancing angles of Ag deposition: mean center-to-center distance between the particles perpendicular to the ripples $L_\perp$ and along the ripples $L_{//}$, normalized correlation lengths $\xi_\perp/L_\perp$ and $\xi_{//}/L_{//}$, peak position (D_1 and D_2) and fwhm (σ_1 and σ_2) of the bimodal lognormal distributions given in figure 5.

Deposition angle (°)	τ_{Ag} (s)	t_{Ag} (nm)	$L_\perp$ (nm)	$\xi_\perp/L_\perp$	$L_{//}$ (nm)	$\xi_{//}/L_{//}$	D_1 (nm)	σ_1 (nm)	D_2 (nm)	σ_2 (nm)	$(L_{//} - D_2)/D_2$
90	6	1.21	9.6	1.6	10.0	1.3	-	-	5.3	4.4	0.89
20	11	1.42	22.8	3.2	11.9	1.0	2.8	3.7	6.7	6.4	0.78
8	17	1.27	23.9	4.2	12.4	1.3	2.4	3.2	7.8	4.0	0.59
2	28	1.40	25.1	3.9	14.0	1.1	2.4	3.2	9.4	4.9	0.49

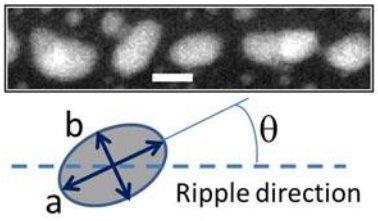

Figure 4: Sketch of the orientation θ of an individual ellipsoidal nanoparticle (with long axis a and short axis b) with respect to the ripple direction (bottom). The scale bar corresponds to 10 nm in the HAADF-STEM image (top).

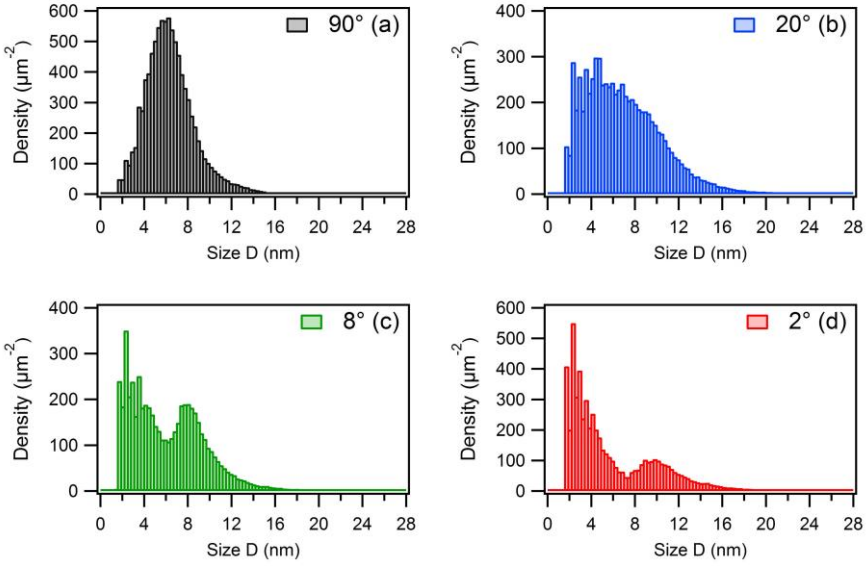

Figure 5: In-plane size *D* distributions for Al_2O_3-capped Ag nanoparticles grown on rippled Al_2O_3 thin films with different glancing angles of Ag deposition: (a) 90°, (b) 20°, (c) 8°, and (d) 2°.

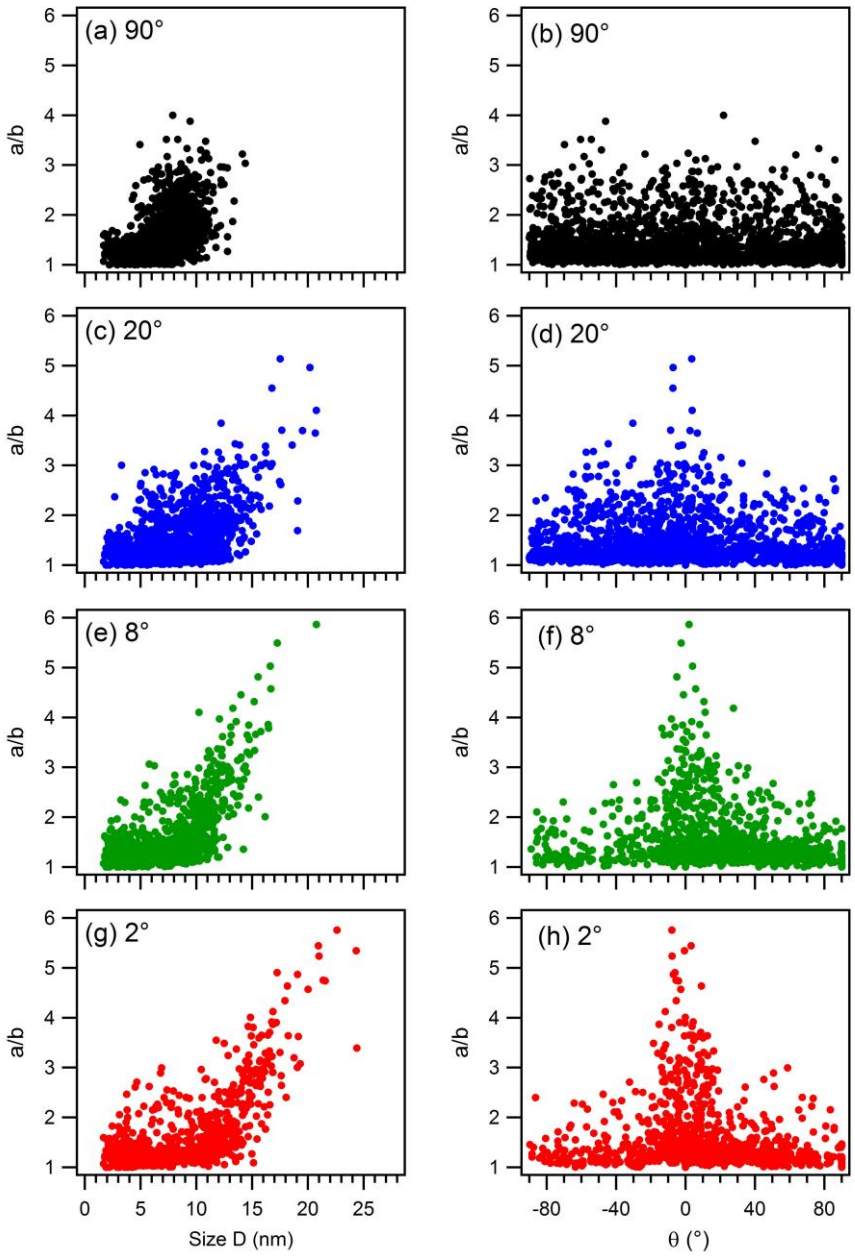

Figure 6: In-plane aspect ratio *a/b* as a function of the size *D* (a,c,e,g) and orientation θ (b,d,f,h) for Al_2O_3-capped Ag nanoparticles grown on rippled Al_2O_3 thin films with different glancing angles of Ag deposition: 90° (a,b), 20° (c,d), 8° (e,f), and 2° (g,h).

3.3. Influence of the pre-patterned surface ordering on the particle growth

Figures 7(a)-7(c) show the in-plane view HAADF STEM images of Al_2O_3-capped Ag nanoparticles grown at a glancing incidence of 2° on pre-patterned Al_2O_3 surfaces with sputtering parameters (600 eV-100 s), (600 eV-1000 s), and (1 keV-100 s), respectively. The corresponding autocorrelation functions given in figures 7(d)-7(f) evidence an improved in-plane organization of the particles when the sputtering time is 1000 s since the periodic fringes become sharper. This is confirmed by GISAXS measurements, as presented in figures 8(a)-8(b), which have to be compared to the GISAXS maps of pre-patterned surfaces shown in figure 2. After Ag deposition and Al_2O_3 capping, the GISAXS maps display asymmetric streaks modulated by fringes along the vertical direction. These fringes arise from interferences between the upward and downward propagating waves into the stratified film and are the signature of the replication of topography of the buried Ag nanoparticles by the surface roughness of the Al_2O_3 capping layer [20, 28]. Furthermore, the asymmetry in the intensity distribution with respect to the q_y axis can be ascribed to the scattering of nanoparticles tilted from the normal to the mean surface, which is consistent with a preferential particle growth on the ripple sides exposed to the Ag flux during the deposition. It is also worth noting that the position and lateral width of the first-order streaks as well as the relative intensity of the second-order streaks exhibit the same features as obtained on the corresponding pre-patterned surfaces. Hence, these statistically averaged data confirm the HAADF-STEM observations suggesting that both the period and ordering of the ripple pattern is replicated by the Ag nanoparticle arrays, which results in a better spatial organization of the particles for long sputtering times during pre-patterning of the Al_2O_3 surface.

As described in the previous section, we carried out a quantitative analysis of the HAADF-STEM images of all the samples prepared using a glancing angle of Ag deposition of 2° and different sputtering parameters (table 3). Again, we consistently found a bimodal distribution of the in-plane size D with a first peak centered at $D_1 \sim 2.3$ nm, while the position of the second one D_2 increases for Ag depositions performed on surfaces prepared with increasing sputtering times. As shown in figure 9 and table 3, this coarsening is associated with an increase of the in-plane aspect ratio a/b of the largest nanoparticles, whose preferential orientation is obviously along the ripples (figure 7(b)), and with an increase of the mean distance $L_{//}$ in the longitudinal direction as well as a decrease of the mean $(L_{//} - D_2)/D_2$ ratio from 0.78 to 0.62. Accordingly, although the mean interparticle distance $L_\perp$ in the transverse direction remains dictated by the ripple period (with $\xi_\perp / L_\perp$ being similar to the value obtained on the pre-patterned surface), the longitudinal growth and ordering of the particles are strongly influenced by the pattern quality. For Ag depositions performed on surfaces prepared with short sputtering times, the high density of local defects such as ripple bifurcations and interstitials [29] results in the formation of poorly organized and slightly elongated nanoparticles. In contrast, Ag

depositions performed on surfaces prepared using longer sputtering times lead to more elongated and more closely spaced nanoparticles by replication of the ripple pattern quality.

Table 3: Structural parameters retrieved from the quantitative analysis of HAADF-STEM images and corresponding autocorrelation functions of Al_2O_3-capped Ag nanoparticles grown at a glancing incidence of 2° on pre-patterned Al_2O_3 thin films prepared using different sputtering parameters "ion energy-sputtering time": mean center-to-center distance between the particles perpendicular to the ripples $L_\perp$ and along the ripples $L_{//}$, normalized correlation length $\xi_\perp/L_\perp$ and $\xi_{//}/L_{//}$, peak position (D_1 and D_2) and fwhm (σ_1 and σ_2) of the corresponding bimodal lognormal distributions.

Sputtering energy (eV)	Sputtering time (s)	$L_\perp$ (nm)	$\xi_\perp/L_\perp$	$L_{//}$ (nm)	$\xi_{//}/L_{//}$	D_1 (nm)	σ_1 (nm)	D_2 (nm)	σ_2 (nm)	$(L_{//}-D_2)/D_2$
600	100	16.9	2.9	10.4	1.2	2.3	2.1	5.8	4.1	0.79
	200	18.4	3.8	11.8	1.2	2.5	2.8	6.9	4.5	0.71
	500	19.8	5.2	13.6	0.9	2.3	2.6	7.8	4.7	0.74
	1000	22.2	4.9	13.8	1.2	2.1	2.4	8.5	4.8	0.62
1000	100	21.1	3.3	11.4	1.1	2.1	2.0	6.2	5.1	0.84

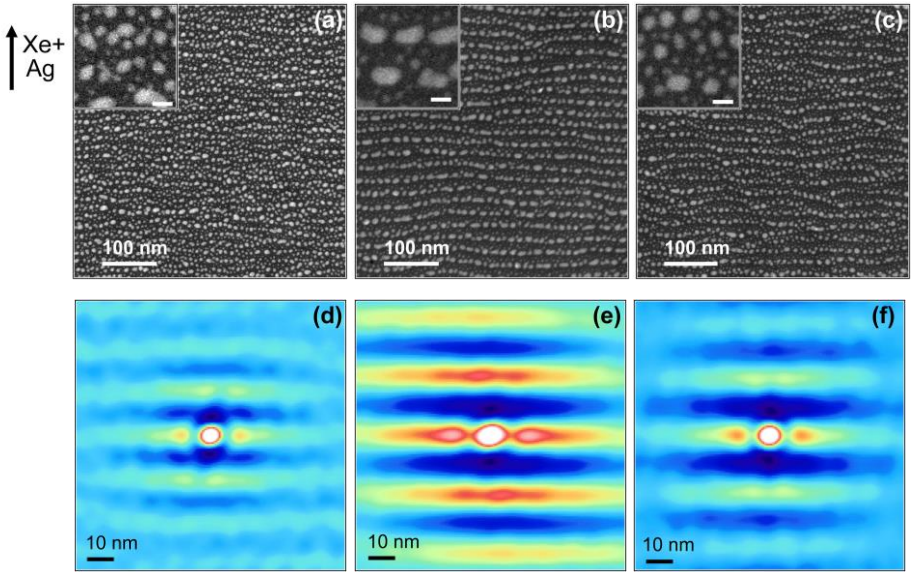

Figure 7: HAADF-STEM plan view images of Al_2O_3-capped Ag nanoparticles grown at a glancing incidence of 2° on pre-patterned Al_2O_3 thin films prepared using different sputtering parameters (a) 600 eV-100 s, (b) 600 eV-1000 s, and (c) 1 keV-100 s. Scale bars in the zoomed portions shown in the insets correspond to 10 nm. (d,e,f) Corresponding autocorrelation functions of images (a,b,c). The direction of the Xe^+ and Ag beam projections are shown by the arrow.

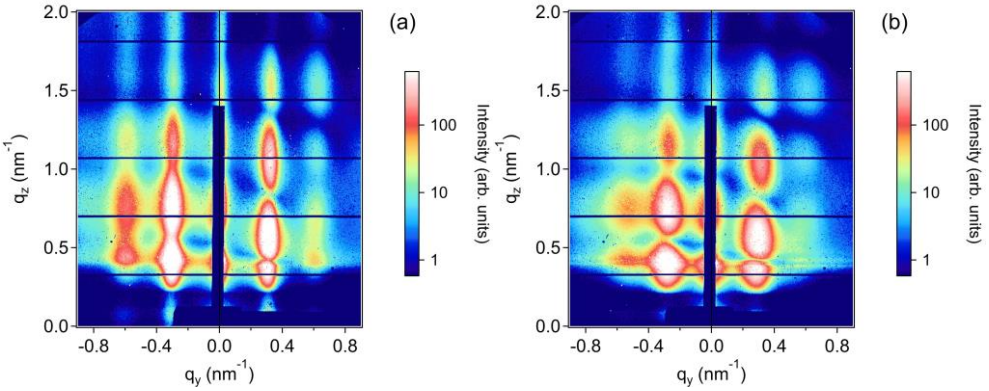

Figure 8: Experimental 2D GISAXS maps obtained for Al_2O_3-capped Ag nanoparticles grown at a glancing incidence of 2° on pre-patterned Al_2O_3 thin films prepared using different sputtering parameters (a) 600 eV-1000 s and (b) 1 keV-100 s.

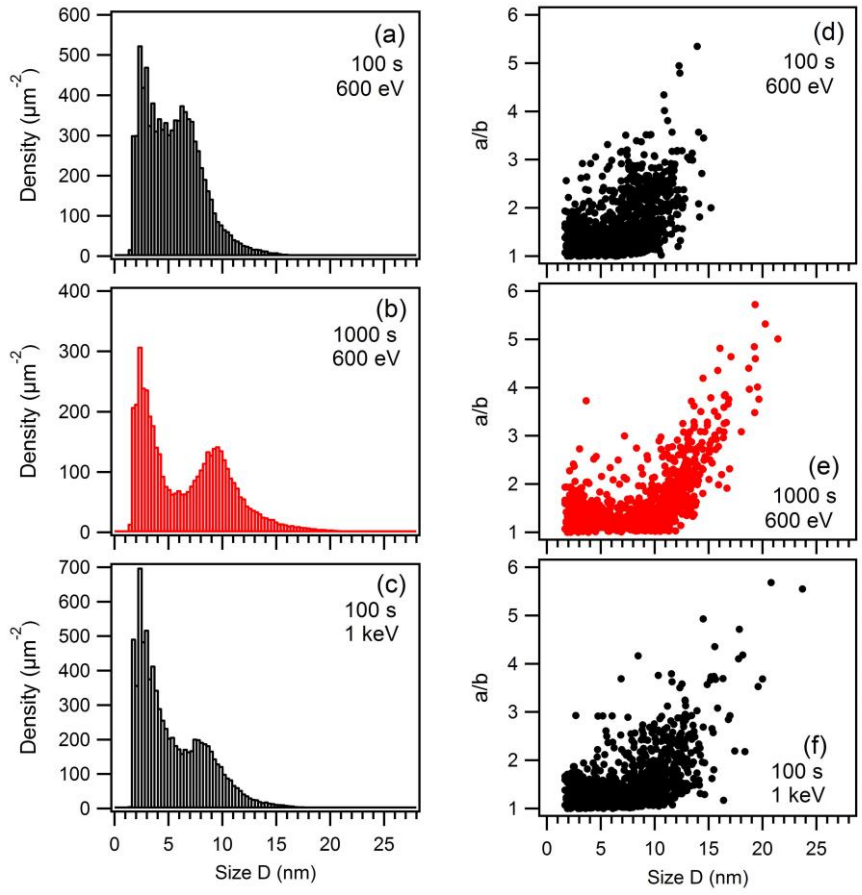

Figure 9: In-plane size *D* distributions for Al_2O_3-capped Ag nanoparticles grown at a glancing incidence of 2° on pre-patterned Al_2O_3 thin films prepared using different sputtering parameters (a)

600 eV-100 s, (b) 600 eV-1000 s, and (c) 1keV-100 s. In-plane aspect ratio a/b as a function of the size D: (d) 600 eV-100 s, (e) 600 eV-1000 s, and (f) 1 keV-100 s.

3.4. Optical properties of the nanoparticle arrays

The optical properties of the $Al_2O_3/Ag/Al_2O_3$ nanocomposite films deposited on SiO_2 substrates were studied by transmission measurements at normal incidence with two polarizations of the incident light, oriented in the longitudinal (//) and transverse (⊥) directions compared to the ripple direction. In all cases, the structural anisotropy results in an optical dichroism, $\lambda_{//} - \lambda_{\perp} \neq 0$, where $\lambda_{//}$ and $\lambda_{\perp}$ are the spectral positions of the minimum of transmittance for longitudinal and transverse polarizations, respectively. Furthermore, this dichroism intensifies as the glancing angle of Ag deposition decreases and the sputtering time increases (table 4). Nevertheless, as shown in figures 10 and 11, the position of the transverse resonance $\lambda_{\perp}$ is relatively constant, in the range from 500 to 520 nm, while the longitudinal resonance $\lambda_{//}$ is more or less shifted to higher wavelengths. Meanwhile, a damping and an inhomogeneous broadening of the longitudinal resonance can be noticed, even though the amplitude and width of the transverse resonance remain stable. Moreover, for a longitudinal excitation, a second resonance centered at a lower wavelength (around 500 nm) is clearly observed when Ag deposition is performed at glancing angles of 2° and 8° onto Al_2O_3 surfaces pre-patterned with long sputtering times. Qualitatively, these results confirm that the dichroic properties of such arrays of elongated nanoparticles are strongly affected by the spatial organization of the particles and, therefore, both by the quality of the underlying ripple pattern and by the glancing angle of Ag deposition. Nevertheless, it can be noticed that the nanoparticle arrays grown on pre-patterned surfaces prepared at 600 eV with sputtering times of 1000 s and 500 s present similar optical properties (figure 11(a)).

Table 4: Spectral position of the minimum of transmittance for transverse ($\lambda_{\perp}$) and longitudinal ($\lambda_{//}$) excitations.

Sputtering energy (eV)	Sputtering time (s)	Deposition angle (°)	$\lambda_{//}$ (nm)	$\lambda_{\perp}$ (nm)	$\lambda_{//} - \lambda_{\perp}$ (nm)
1000	300	90	528	517	11
		20	559	522	37
		8	608	502	106
		2	688	498	190
	100	2	626	510	116
600	100	2	579	516	63
	200		607	520	87
	500		679	516	163
	1000		680	514	166

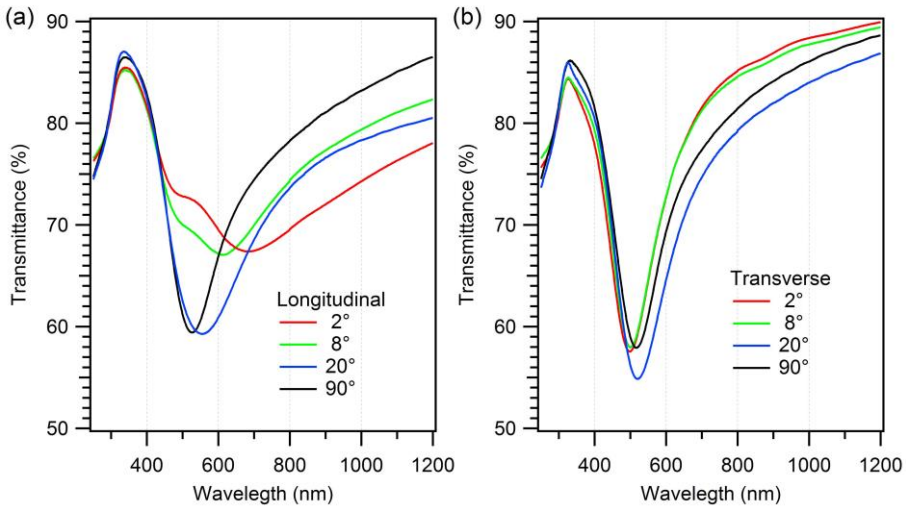

Figure 10 : Transmission measurements at normal incidence with two polarizations of the incident light, oriented in the longitudinal (a) and transverse (b) directions compared to the ripple direction, for Al_2O_3-capped Ag nanoparticles grown on rippled Al_2O_3 thin films with different glancing angles of Ag deposition: 90°, 20°, 8° and 2°.

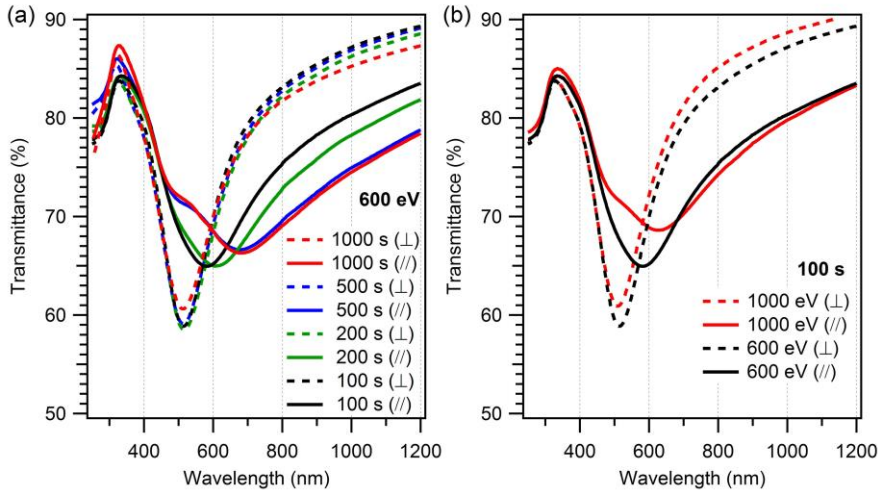

Figure 11: Transmission measurements at normal incidence with two polarizations of the incident light, oriented in the longitudinal (solid lines) and transverse (dotted lines) directions compared to the ripple direction, for Al_2O_3-capped Ag nanoparticles grown at a glancing incidence of 2° on pre-patterned Al_2O_3 thin films prepared using different sputtering parameters: (a) 600 eV-100 s, 600 eV-200 s, 600 eV-500 s, and 600 eV-1000 s; (b) 600 eV-100 s and 1keV-100 s.

4. Discussion

For an individual metallic nanoparticle, the spectral position of the LSPR is determined by its size and shape, and by the properties of the metal and external dielectric environment around it (i.e. the dielectric host). The particle can exhibit dipolar excitations with triple degeneracies for an ellipsoidal shape, and therefore three resonances whose spectral positions depend on the ellipsoid aspect ratio. For example, an ellipsoidal Ag nanoparticle embedded in an Al_2O_3 matrix (n = 1.65 at 633 nm) with in-plane axes a = 10 nm, b = 8 nm, and out-of-plane axis c = 5 nm presents three LSPR located at λ_a = 565 nm, λ_b = 490 nm, and λ_c = 390 nm, respectively, while a spherical particle with $a = b = c$ = 10 nm presents a unique LSPR at 455 nm and a spheroidal particle with $a = b$ = 10 nm and c = 5 nm exhibits two LSPR at $\lambda_a = \lambda_b$ = 545 nm and λ_c = 380 nm. For a system of two or more nanoparticles close enough to each other (e.g. a linear chain), a new phenomenon arises as a result of plasmon coupling, which produces a significant change of the optical response of the nanocomposite. Indeed, when identical nanoparticles are close to each other within a linear chain, they interact via their radiative electric field and the interaction between neighbors can produce mixing and splitting of the dipolar modes of each particle [30-33]. According to the polarization of the incident electric field with respect to the direction of the nanoparticle chain, a small blue-shift (for a transverse polarization) or a red-shift (for a longitudinal polarization) is produced when compared with an isolated nanoparticle. The magnitude of the red-shift becomes more significant as the gap between the particles decreases, while the one of the blue-shift is almost undetectable. Furthermore, some authors have shown that multipolar terms become relevant in the effective response of closely spaced nanoparticles, adding resonances at wavelengths lower than the dipolar mode [34-38]. Accordingly, as mentioned in the introduction, a key parameter which controls the optical behavior of a regular array is the gap between particles compared to their size.

Compared to nanolithography techniques, the main drawback of IBS for any practical application is the difficulty in obtaining monodisperse arrays of nanoparticles with regular morphology and interparticle distance. Nevertheless, as shown in figures 3 and 7, by combining a long sputtering time for ripple formation and a low glancing angle for Ag deposition, the interparticle gaps inside the periodic chains (i.e. along the longitudinal direction) can decrease down to 1 nm or even less, and may vary up to a few nm. In order to study the influence of such small and polydisperse gaps, we performed Finite Difference Time Domain (FDTD) calculations with Lumerical software [39], as presented in figures 12, 13 and 14. Within the frame of a classical electromagnetic model, we simulated the optical response of two pairs of Ag nanoparticles embedded in an Al_2O_3 matrix, the nanocomposite layer being supported on a SiO_2 substrate (figure 12(a)). To simplify the problem, we considered identical ellipsoidal nanoparticles with in-plane axes a = 10 nm and b = 8 nm corresponding to average experimental values. Furthermore, since the experimental out-of-plane

aspect ratio *c/D* is expected to be smaller than one [26], we fixed the out-of-plane axis *c* to 5 nm. The complex refractive indices of Ag and Al_2O_3 were obtained by spectroscopic ellipsometry measurements, in the visible range (400 nm-800 nm), of thick films deposited on a silicon substrate by IBS. The distance between the two pairs in the transverse direction was set to 23 nm (i.e. equivalent to the ripple period), while the gap *g* between two adjacent particles was varied from 10 nm to 0.5 nm in the longitudinal direction. We considered periodic boundary conditions of the FDTD simulation domain in the (x,y) plane and Perfectly Matched Layer (PML) boundary conditions in the z-direction, with a graded mesh region. A mesh override region, with a cubic mesh size of 0.1 nm×0.1 nm×0.1 nm, was considered for simulation domain close to the nanoparticles. The incident source, located in the substrate region, was considered as a plane wave source with amplitude E_0 equal to 1 V/m and with a polarization direction either parallel or perpendicular to the pair axis (x-direction). When the polarization of the incident light is transverse to the pair axis, the spectral position of the LSPR, $\lambda_\perp$, is weakly dependent on the particle gap in the longitudinal direction and is similar to the one obtained for an isolated ellipsoidal nanoparticle: $\lambda_\perp$ = 505 nm for $g = a$ = 10 nm and $\lambda_\perp$ = 500 nm for $g = a/10$ = 1 nm (not shown). It is worth noting that these calculated $\lambda_\perp$ values are consistent with our experimental results. Moreover, as also observed experimentally, reducing the distance $L_\perp$ between the two-particle pairs from 23 nm to 15 nm does not affect the spectral shape and position of the transverse resonance because the particles present an edge-to-edge distance ($L_\perp - b$) larger than their dimension *b* in this direction. On the contrary, when the incident electric field is polarized along the pair axis, the longitudinal resonance is strongly dependent on the particle gap *g* as shown in figures 12(b) and 13(a). For $g = a$ = 10 nm, the interactions between the particles are weak and therefore the transmission spectrum is similar to the one obtained with a single particle (dipole mode). As *g* decreases, the longitudinal resonance gradually shifts to the red due to an enhancement of the particle coupling, the LSPR position being shifted to $\lambda_{//}$ = 665 nm for near touching particles (g = 0.5 nm). Furthermore, as indicated by an arrow in figure 12(b), when g = 1 nm = $a/10$, a new band of absorption with much lower amplitude becomes apparent at lower wavelength (~ 500 nm) that also red-shifts as the particles get closer. This new mode is the signature of bonding hybridized quadrupolar resonance. Nevertheless, let us note that for gaps smaller than 0.5 nm and larger than 0.1 nm, quantum mechanical effects may play an important role and therefore the classical description breaks down [40, 41]. In these conditions, the electron tunneling probability increases as the gap decreases and hence a less pronounced red-shift with a reduction of the field enhancement is expected. For gaps smaller than 0.1 nm, a conductive overlap is established between the nanoparticles (conductive regime) and a new plasmon mode is enabled, the charge transfert plasmon [38] that involves conduction electrons flowing back and forth between the particles. As shown in figure 13(a), calculations made with two pairs of spheroidal nanoparticles (with $a = b$ = 10 nm and c = 5 nm) and spherical nanoparticles (with $a = b = c$ = 10 nm) not only confirm the blue-shift of the longitudinal

resonance compared to ellipsoidal particles, but also the red-shift as *g* decreases. They also show the appearance of a small absorption band at lower wavelength for near touching nanoparticles (e.g., for *g* = 1 nm, a shoulder in the transmission spectra appears at 525 nm and at 460 nm for spheroidal and spherical particles, respectively). In figure 13(b), the maximum of the field enhancement $|E/E_0|_{max}$ obtained at the LSPR for a longitudinal excitation is plotted versus the particle gap *g*. For *g* = 10 nm, $|E/E_0|_{max}$ is close to the value obtained for a single particle (referenced by the dotted line for an ellipsoidal nanoparticle), while $|E/E_0|_{max}$ strongly increases as *g* decreases, owing to an increase of the particle interactions. In this case, the electromagnetic field is highly confined within the interstice between the particles, as shown in the insets of figure 13(b) where field enhancement $|E/E_0|$ maps are given for *g* = 10 nm and 1 nm. Furthermore, the maximum of the field enhancement $|E/E_0|_{max}$ at the LSPR is always slightly higher for ellipsoidal particles than for spheroidal and spherical particles, whatever the gap *g* [42]. At last, it is worth noting that the spectral position of the minimum of transmittance (that is measured in far field) in the longitudinal direction strongly depends on the number of particles inside a linear chain (figure 14) [43]. Overall, the longitudinal resonance shifts to the red when increasing the number of particles. This effect is particularly pronounced for 3 or 4 particles compared to a pair of particles and also more important for gaps smaller than 1 nm, implying that the interactions between the nanoparticles extend beyond the first nearest neighbor, the extension being larger for small gaps [44]. Therefore, the gap distribution inside the chains of particles is expected to have a crucial impact on the macroscopic optical response of the nanoparticle array.

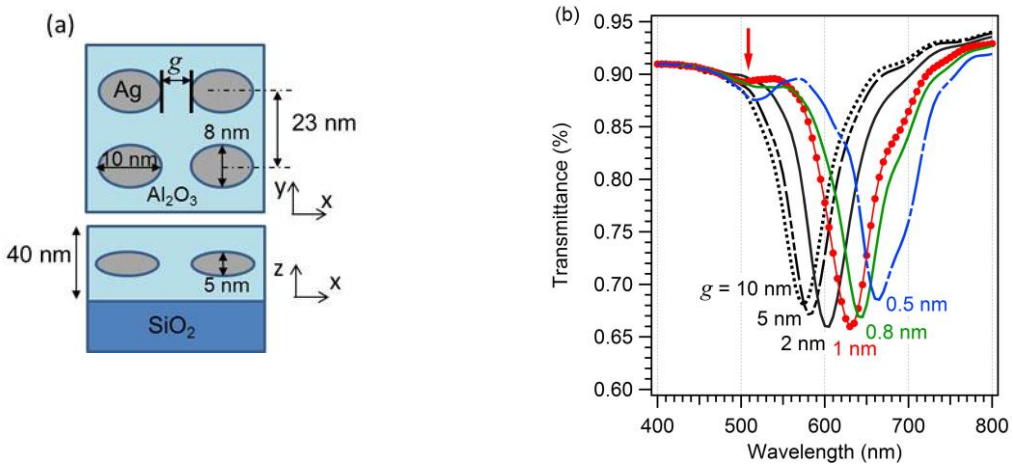

Figure 12: (a) Sketch of the configuration used to perform FDTD calculations for two pairs of identical ellipsoidal Ag nanoparticles surrounded by an Al_2O_3 matrix deposited on a SiO_2 substrate. (b) Calculated transmission at normal incidence for a longitudinal excitation (i.e. for a polarization of the

electric field along the x-direction). The gap g between the two ellipsoidal particles is reduced from 10 nm to 0.5 nm. The red arrow indicates the emergence of a second absorption band for g = 1 nm.

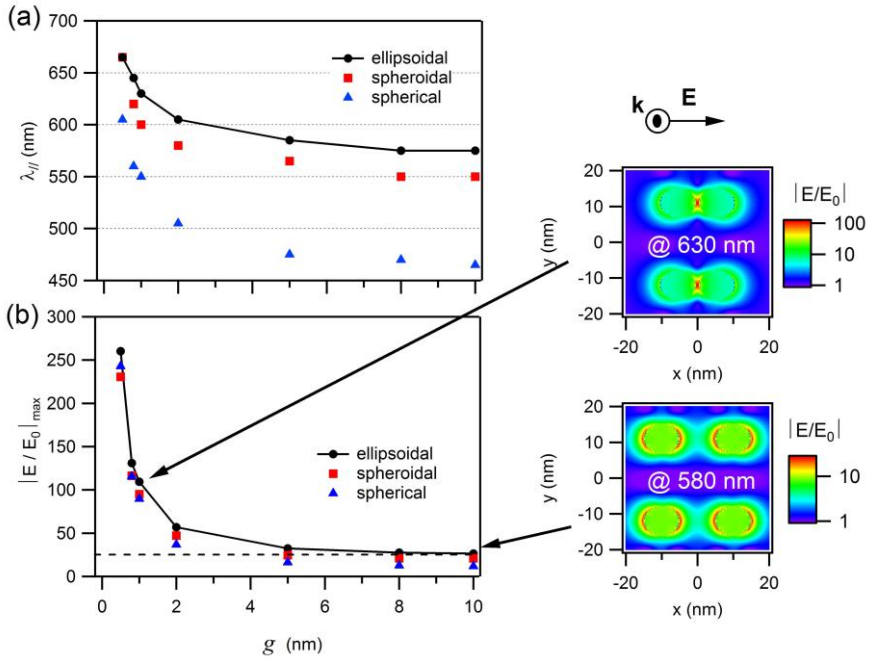

Figure 13: (a) Variations of the spectral position of the dipolar longitudinal resonance as a function of the interparticle gap g for ellipsoidal, spheroidal and spherical nanoparticles (see text). (b) Variations of the maximum of the field enhancement $|E/E_0|$, obtained at the LSPR for a longitudinal excitation, as a function of the interparticle gap g for ellipsoidal, spheroidal and spherical nanoparticles (see text). The dashed line corresponds to the $|E/E_0|$ value obtained for a single ellipsoidal particle. Insets: field enhancement $|E/E_0|$ maps calculated for g = 10 nm at $\lambda_{//}$ = 580 nm and for g = 1 nm at $\lambda_{//}$ = 630 nm.

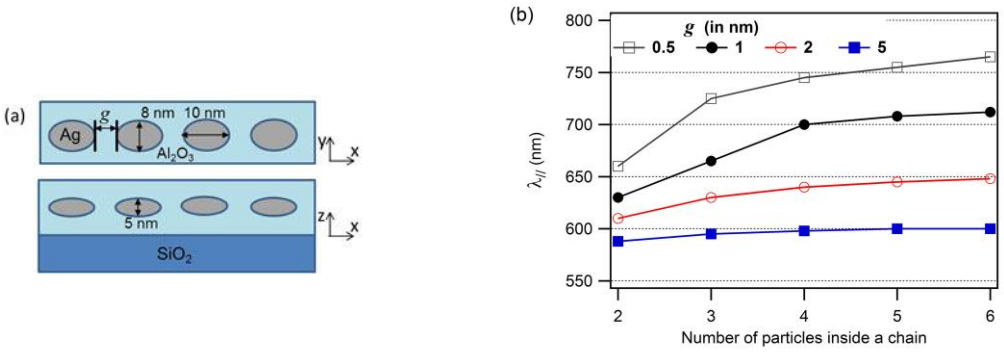

Figure 14: (a) Sketch of the configuration used to perform FDTD calculations for a linear chain of identical ellipsoidal Ag nanoparticles surrounded by an Al_2O_3 matrix deposited on a SiO_2 substrate. (b) Variations of the spectral position of the minimum of transmittance, calculated at normal incidence for a longitudinal excitation, as a function of the number of particles inside the chain for interparticle gaps g = 5, 2, 1 and 0.5 nm.

Compared to our experimental observations, this numerical study confirms that for normal incidence deposition, the slight dichroism ($\lambda_{// 90°} - \lambda_{\perp 90°} = 11$ nm) originates from the dipolar modes (longitudinal and transverse) of slightly ellipsoidal particles, far to each other. Combining long sputtering times for ripple formation (≥ 300 s) and low glancing angles for Ag deposition (≤ 8°), only one narrow band associated to a dipole transverse plasmon resonance is observed experimentally when the incident polarization is perpendicular to the nanoparticle chains because the mean interparticle distance $L_\perp$ is imposed by the ripple period and is much larger than the particle dimension in this direction. In contrast, two absorption bands are observed when the polarization is parallel to the nanoparticle chains (figure 10(a)). The more intense of these two longitudinal LSPR exhibits a prominent red-shift as the deposition angle decreases. According to our simulations (figures 12-14), this behavior may be related to the chaplet-like organization of elongated particles together with the reduction of the mean gap between particles. Moreover, the experimental broadening and damping of this "red resonance" may arise from the development of a broad distribution of small gaps (g < 2 nm) within the nanoparticle chains since weak gap variations induce large red-shifts of the resonance (even if shape distribution may also contribute to the broadening of the resonance). The less intense of the two longitudinal LSPR appears at a lower and nearly constant wavelength around 500 nm ("blue resonance"), while its amplitude decreases as the deposition angle decreases. Although the contribution of quadrupolar resonances cannot be ruled out, the "blue resonance" is most likely to arise from the presence of a significant number of particles randomly oriented and distributed on the surface. Accordingly, owing to the formation of less elongated and more spaced particles in the ripple direction, Ag depositions performed either at high glancing angles or on pre-patterned surfaces prepared with short sputtering times generate a single longitudinal LSPR that is indeed caused by the contribution of two populations: i) particles randomly oriented and "optically" isolated ("blue resonance" always peaking at ~ 500 nm) and ii) particles oriented in the direction parallel to the ripples and "optically" coupled ("red resonance" whose spectral position shifts to lower wavelengths as the deposition angle increases or the sputtering time decreases). Obviously, the formation of aligned and elongated particles with sub-nanometer gaps promotes coupling between particles, and hence leads to strong electric field enhancements (figure 13). Furthermore, our experimental results and numerical simulations suggest that the spectral position of the "red resonance" observed for a longitudinal excitation is a signature of

this coupling, i.e. strongly coupled elongated particles are expected to generate a longitudinal LSPR at higher wavelengths than isolated spherical particles.

5. Conclusion

In this paper, we have demonstrated that low-energy ion beam sputtering of a dielectric surface followed by Volmer-Weber growth of metallic nanoparticles by physical vapor deposition at glancing angles is a versatile method that can be optimized in order to produce nanoparticle arrays with dimensions and gaps below the resolution of lithographic techniques. It is reliable, easy to apply at low cost and at wafer scale. Since the nanoparticles can be protected from atmospheric exposure by a capping layer of controlled thickness, all the surfaces possess high stability and can be easily cleaned without modifications of their properties. The quality of the ripples and the angle of metal deposition are key factors in the nanoparticle growth mechanisms. We have shown that a long sputtering time for ripple formation (i.e. a high ion fluence) and a low glancing angle for metal deposition favor the formation of aligned and elongated nanoparticles with sub-nanometer interparticle gaps. These nanoparticle arrays generate high electric field enhancements for a longitudinal excitation and therefore could be employed as reusable substrates for surface enhanced spectroscopies in routine analysis. In addition, since IBS has proved its applicability to a wide range of materials, the spectral position of the longitudinal resonance could be adjusted via the dielectric functions of the pre-patterned buffer layer and capping layer. Thus, the optical properties of the nanoparticle arrays could be optimized for various SERS excitation wavelength/molecule combinations.

Acknowledgments:

The authors want to thank Dr. G. Abrasonis from Helmholtz-Zentrum (Dresden-Rossendorf, Germany) for performing RBS measurements, the ESRF-D2AM beamline staff (Grenoble, France) for experimental support during GISAXS experiments and Dr. F. Pailloux (Institut Pprime, France) for assistance during HAADF-STEM measurements. This work has been carried out within the QMAX project No. ANR-09-NANO-031 funded by the French National Agency (ANR) in the frame of its 2009 programme in Nanosciences,Nanotechnologies and Nanosystems (P3N2009) and has been also funded by C'Nano (Centre de compétences en Nanosciences).

References

1. Kreibig U and Volmer M 1999 *Optical Properties of Metal Clusters*, (Springer, Berlin)
2. Bohren C F and Huffman D R 1983 *Absorption and Scattering of Light by Small Particles*, edited by Bohren C F and Huffman D R (Wiley, New York)
3. Kelly K L, Coronado E, Zhao L L and Schatz G C 2003 *J. Phys. Chem. B* **107** 668
4. Noguez C 2007 *J. Phys. Chem. C* **111** 3806
5. Khlebtsov N G and Dykman L A 2010 *J. Quant. Spec. Rad. Trans.* **111** 1–35
6. Fan M K, Andrade G F S and Brolo A G 2011 *Analytica Chimica Acta*, **693** 7-25
7. Cialla D, März A, Böhme R, Theil F, Weber K, Schmitt M and Popp J 2012 *Analytical and Bionanalytical Chemistry* **403** 27-54
8. Guillot N and de la Chapelle M L 2012 *Journal of Nanophotonics* **6** 064506
9. Muñoz-Garcia J, Vasquez L, Cuerno R, Sanchez-Garcia J A, Castro M and Gago R 2009 *Towards Functional Nanomaterials*, edited by Z. M. Wang (Springer, New York) p 323–398
10. Chan W L. and Chason E J. 2007 *Appl. Phys.* **101** 121301
11. Valbusa U, Boragno C and Buatier de Mongeot F 2002 *J. Phys.:Condens. Matter* **14** 8153
12. Makeev M A, Cuerno R and Barabasi A L 2002 *Nucl. Instrum.Methods Phys. Res., Sect. B* **197** 185
13. Oates T W H, Keller A, Facsko S and Mücklich A 2007 *Plasmonics* **2** 47
14. Oates T W H, Keller A, Noda S and Facsko S 2008 *App. Phys. Let.* **93** 063106
15. Toma A, Chiappe D, Massabo D, Boragno C and de Mongeot F B 2008 *Appl. Phys. Lett.* **93** 163104
16. Camelio S, Babonneau D, Lantiat D, Simonot L and Pailloux F 2009 *Phys. Rev. B* **80** 155434
17. Babonneau D, Camelio S, Simonot L, Pailloux F, Guérin P, Lamongie B and Lyon O 2011 *Europhys. Lett*. **93** 26005
18. Camelio S, Babonneau D, Pailloux F, Rousselet S, Vandenhecke E 2013 *Nanoscience and Nanotechnology Letters* **5** 19
19. Ranjan M and Facsko S 2012 *Nanotechnology* **23** 485307
20. Babonneau D, Camelio S, Vandenhecke E, Rousselet S, Garel M, Pailloux F and Boeseke P 2012 *Phys. Rev. B* **85** 235415

    Babonneau D, Camelio S, Vandenhecke E, Rousselet S, Garel M, Pailloux F and Boeseke P 2013 *Phys. Rev. B* **87** 159903(E)

21. Ziberi B, Frost F, Höche Th and Rauschenbach B 2005 *Phys. Rev. B* **72** 235310
22. Umbach C C, Headrick R L and Chang K C 2001 *Phys Rev Lett.* **87**, 246104

23. Zhou H, Wang Y, Zhou L, Headrick R L, Özcan A S, Wang Y, Özaydin G and Ludwig K F 2007 *Phys. Rev. B* **75** 155416
24. Headrick R L and Zhou H 2009 *J. Phys.: Condens Matter* **21** 224005
25. Toudert J, Camelio S, Babonneau D, Denanot M F, Girardeau T , Espinos J P, Yubero F, and Gonzalez-Elipe A R 2005 *J.Appl. Phys.* **98** 114316
26. Lantiat D, Babonneau D, Camelio S, Pailloux F and Denanot M F 2007 *J. Appl. Phys.* **102** 113518
27. Numazawa S, Ranjan M, Heinig K H, Facsko S and Smith R 2011 *J. Phys.: Condens. Matter* **23** 222203
28. Babonneau D, Camelio S, Lantiat D, Simonot L and Michel A 2009 *Phys. Rev. B* **80**, 155446
29. Keller A and Facsko S 2010 *Phys. Rev. B* **82** 155444
30. Rechberger W, Hohenau A, Leitner A, Krenn J R, Lamprecht B and Aussenegg F R 2003 *Optics Communications* **220** 137
31. Jain P K, Huang W and El-Sayed M A 2007 *Nano Lett.* **7** 2080-88
32. Jain P K and El-Sayed M 2008 *J. Phys. Chem. C.* **112** 4954–60
33. Liu Z, Boltasseva A, Pedersen R H, Bakker R, Kildishev A V,. Drachev V P and Shalaev V M 2008 *Metamaterials* **2** 45–51
34. Atay T, Song J-H and Nurmikko A V 2004 *Nano Lett.* **4** 1627-31
35. Enoch S, Quidant R and Badenes G 2004 *Optics Express* **12** 3422
36. Romero I, Aizpurua J, Bryant G W and García de Abajo F J 2006 *Optics Express* **14** 9988
37. Encina E R and Coronado E A 2010 *J. Phys. Chem. C* **114** 3918–3923
38. Chern R-L, Liu X-X and Chang C-C 2007 *Phys. Rev. E* **76** 016609
39. Lumerical Solutions, Inc. Available: http://www.lumerical.com
40. Esteban R, Borisov A G, Nordlander P and Aizpurua J 2012 *Nat. Comm.* **3**, 825
41. Zuloaga J, Prodan E and Nordlander P 2009 *Nano Lett.* **9**, 887-891
42. Norton S J and Vo-Dinh T 2008 *J. Opt. Soc. Am. A* **25** 2767
43. Barrow S J, Funston A M, Gomez D E, Davis T J and Mulvaney P 2011 *Nano Lett.* **11** 4180–4187
44. Sweatlock L A, Maier S A, Atwater H A, Penninkhof J J and Polman A 2005 *Phys. Rev. B* **71** 235408